JOURNAL OF GEOPHYSICAL RESEARCH, VOL. 99, NO. C9, PAGES 18,255–18,273, SEPTEMBER 15, 1994

Mean sea surface height of the Antarctic Circumpolar Current from Geosat data: Method and application

Sarah T. Gille
Massachusetts Institute of Technology/Woods Hole Oceanographic Institution, Woods Hole, Massachusetts

Abstract. The mean sea surface height across the Antarctic Circumpolar Current has been reconstructed from height variability measured by the Geosat altimeter without assuming prior knowledge of the geoid. For this study, an automated technique has been developed to estimate mean sea surface height for each satellite ground track using a meandering Gaussian jet model, and errors have been estimated using Monte Carlo simulation. The results are objectively mapped to produce a picture of the mean Subantarctic and Polar Fronts, which together comprise the major components of the Antarctic Circumpolar Current. The meandering jet model explains between 40% and 70% of the height variance along the jet axes. The results show that the fronts are substantially steered by topography and that the jets have an average Gaussian width of about 44 km in the meridional direction and meander about 75 km to either side of their mean locations. The average height difference across the Subantarctic Front (SAF) is 0.7 m and across the Polar Front (PF) 0.6 m. The mean widths of the fronts are correlated with the size of the baroclinic Rossby radius.

1. Introduction

The Southern Ocean, the part of the world's oceans south of 35°S, makes up over a quarter of the global ocean surface area. It carries a strong circumpolar flow, the Antarctic Circumpolar Current (ACC), with a total transport of about 130×10^6 m^3 s^{-1}, which represents most of the mass transport between the Atlantic, Pacific, and Indian Oceans.

Despite its substantial transport, the Southern Ocean remains one of the more enigmatic of ocean systems. Owing to remote location, vast size, and consistently poor weather, it has not been sampled extensively using traditional methods. Southern Ocean hydrographic station separations along synoptic sections are often 100 km or more, and sections may be separated spatially by several hundred kilometers and temporally by many years, meaning that mesoscale features are poorly resolved. Historic hydrographic data for the region have been assembled by *Gordon et al.* [1982] and more recently by *Olbers et al.* [1992] to produce relatively consistent, though heavily smoothed and nonsynoptic, pictures of the ACC frontal structure. On the basis of available observations, the ACC is often conceptualized as containing a series of sharp temperature and density fronts, each separating two distinct water masses and supporting a jetlike geostrophic velocity structure [*Nowlin and Klinck,* 1986]. Although some investigators have considered the fronts primarily as water mass separations and have concentrated on temperature and salinity characteristics of the fronts, for the purposes of this investigation they will be identified based on their intensified geostrophic velocities. From north to south, these fronts are referred to as the Subtropical Front (STF), the Subantarctic Front (SAF), the Polar Front (PF), and the Continental Water Boundary (CWB) [*Nowlin and Klinck*, 1986]. The northernmost front, the STF, is blocked by continental boundaries and so carries no circumpolar flow, while the CWB accounts for only about 15% of the ACC transport. (Recent work by *Orsi* [1993] has also suggested the presence of a southern ACC front located between the PF and the CWB.) Together the central SAF and PF carry the bulk of the transport relative to 2500 m through the Drake Passage [*Nowlin and Clifford*, 1982]. Their mean locations, indicated in Figure 1, were estimated by identifying dynamic height gradient maxima in *Gordon et al.*'s [1982] atlas data and smoothed using a biharmonic spline.

Although the observations suggest that the fronts have meandering mesoscale structures, outside of the Drake Passage few moorings have been deployed and few sections have been repeated on a regular basis, so that the data archives contain little information about means and variances of jet locations and transports. As part of International Southern Ocean Studies (ISOS), current meters [*Whitworth et al.*, 1982], heavily instrumented transport moorings [*Whitworth*, 1983; *Whitworth and Peterson*, 1985] and pressure gauges [*Wearn and Baker*, 1980] were deployed across the Drake Passage to monitor the variability of the ACC. Results in-

Paper number 94JC01172.
0148-0227/94/94JC-01172$05.00

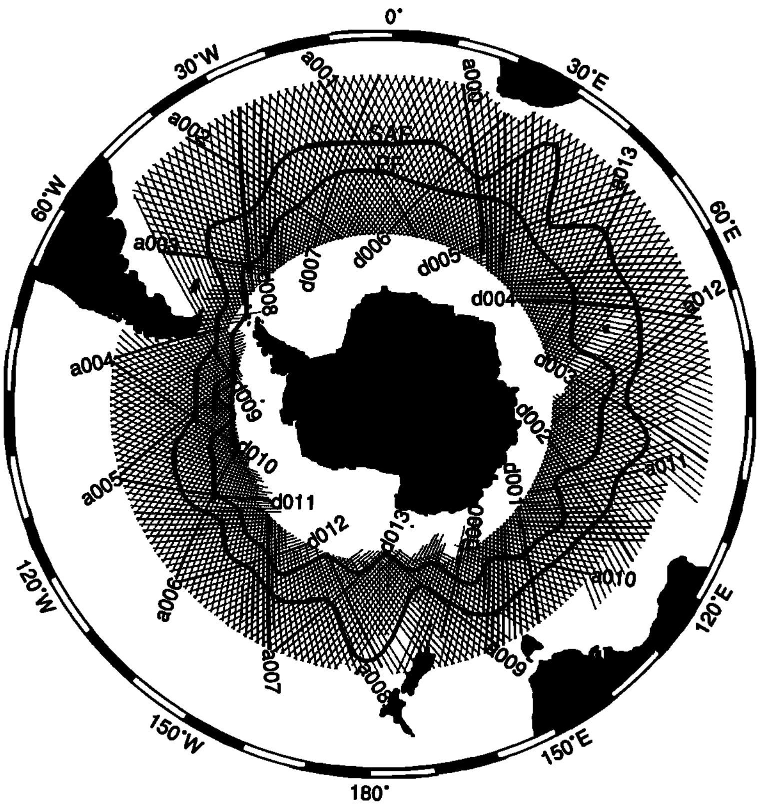

Figure 1. Mean locations of the Subantarctic Front (SAF) and Polar Front (PF), estimated from *Gordon et al.*'s [1982] atlas data, are depicted as bold lines. The medium lines indicate the locations of the 28 track segments, labeled a000 through a013 and d000 through d013, used to select appropriate corrections to apply and for the Monte Carlo error estimations. The lightest lines indicate coverage provided by the 244 ascending and 244 descending Geosat track segments used to reconstruct the mean sea surface height for the Southern Ocean. The outer edge of the map is at 30°S.

dicated that the baroclinic transport is relatively stable, while the barotropic transport fluctuates on the order of 50×10^6 m^3 s^{-1}, with a standard deviation of 10×10^6 m^3 s^{-1}. In a few cases, wave growth and ring formation events have been observed in roughly synoptic expendable bathythermography (XBT) and hydrographic surveys at Drake Passage [*Joyce and Patterson*, 1977; *Peterson et al.*, 1982] and south of Australia [*Savchenko et al.*, 1978], but little information has been available to investigate variability throughout the Southern Ocean. One tool which has proved useful for synoptic studies of mesoscale structures in the Gulf Stream and the Kuroshio, advanced very high resolution radiometer (AVHRR) sea surface temperature data, is of extremely limited use in the Southern Ocean because of the nearly constant cloud cover in the region.

Altimetry provides global measurements of sea surface height (SSH) with relatively dense spatial and temporal coverage. The Geosat Exact Repeat Mission (November 1986 through September 1989) passed over the same collinear tracks every 17 days, providing measurements with 7-km along-track resolution and about 100-km spacing between tracks. The dominant signal in the altimeter data, the Earth's gravitational field (referred to as the geoid), is not known with sufficient accuracy to permit its simple removal from the altimeter measurements. Most investigators have chosen to remove the mean from the data, in essence subtracting the mean SSH along with the geoid, to leave only the variability. Studies by *Chelton et al.* [1990], *Morrow et al.* [1992], and *Johnson et al.* [1992] have taken advantage of Geosat altimeter measurements to investigate SSH variability in the Southern Ocean. This paper will take a slightly different strategy by using the variability along with a Gaussian model of the zonal jet structure to reconstruct the mesoscale mean SSH field. Because of the large quantity of data provided by the altimeter and the sampling problems inherent in the altimeter orbit patterns, a robust and automated data processing scheme has been developed. This approach will allow us to address several lingering issues in the description of basic ACC circulation: Are the altimeter measurements consistent with the idea that the ACC contains continuous narrow jets? Where are these jets located, how far do they meander, how wide are they, and what is the height difference across the jets?

This paper is organized as follows: section 2 (along with the appendix) outlines the basic methodology used to estimate the mean SSH from Geosat data. Section 3 describes the Monte Carlo simulation approach to error analysis. Section 4 presents the objective mapped SSH obtained using this approach. Section 5 focuses specifically on the results, discussing the statistics of jet meandering and carefully examining the reconstructed mean height field. The results are summarized in section 6.

2. Processing the Geosat Data

Collinear Methods and Data Corrections

Altimeter SSH measurements consist of three main components: the geoid, which may change by 30 m across the width of the Southern Ocean; the time-invariant mean oceanographic SSH of 1 to 1.5 m amplitude; and the time-varying fluctuations, typically 0.3 to 0.6 m for mesoscale phenomena. Additional signals are due to orbit error, atmospheric effects, tides, and instrument noise. The basic collinear data processing method may be summarized as follows: For each satellite pass along a given ground track, 30° arcs are selected and missing and out-of-range data points are removed. Data from regions less than 2000 m deep are eliminated because the tidal model is not reliable in shallow water. (This step is omitted in a few cases, notably for ascending tracks near Campbell Plateau, where near-coastal data are needed to identify the ACC.) Selected corrections are applied to the raw data, obvious anomalous spikes are removed, and the data are splined to a common grid. Orbit errors are removed by fitting the height profile to a sinusoid with a wavelength corresponding to one satellite revolution about the Earth. This fit also removes long-wavelength tidal errors and other measurement errors. To prevent regions of large mesoscale variability from biasing the orbit correction, the least squares fit is weighted by the inverse of the height variance. Next the mean height for all of the satellite passes over each point along the orbit is computed and subtracted from the measured height for each satellite pass to produce a time series of residual SSH. The resulting along track data are low-pass filtered. Further details about the collinear method are provided by *Caruso et al.* [1990]. A segment of a filtered time series for one collinear track is shown in Figure 2 (left).

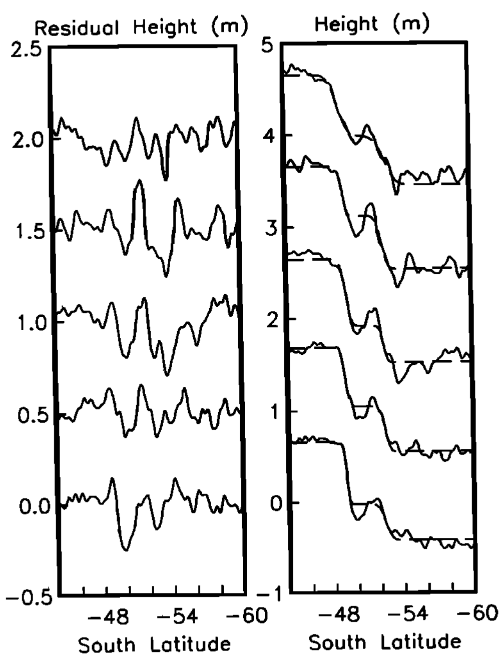

Figure 2. An example time series of (left) residual height data (in meters), and (right) residual height data added to the reconstructed mean (in meters), for the first five satellite passes along track d001. The dashed lines in the right panel indicate instantaneous modeled height from the error function model.

Table 1. The Effect of Each of the Suggested Corrections on the Variance of 28 Ground Tracks

Correction	Mean Variance Change 10^{-4} m^2
None	0.00
Solid earth tide	−3.70
Ionospheric	1.26
Wet troposphere (FNOC)	−3.97
Wet troposphere (SSMI)	−3.73
EM bias	94.41
Inverted barometer	−156.63
Dry troposphere (FNOC)	−50.78
Dry troposphere (ECMWF)	−54.95
Ocean tides	−172.55
Applied corrections	−287.22
All available	−292.43

Ground tracks are referred to as d000 through d013 and a000 through a013 in Figure 1. Numerical values represent the mean change in the variance for all of the points in the 28 tracks.

Standard data corrections are available for solid earth tides, ocean tides, ionospheric effects, dry tropospheric travel time delays (from both the European Center for Medium-Range Weather Forecasting's (ECMWF) operational forecast model and the Fleet Numerical Oceanographic Center's (FNOC) data archives), and wet tropospheric travel time delays (from the special sensor microwave imager (SSMI) and FNOC) [*Cheney et al.*, 1991]. To test their usefulness, each of the corrections was applied to data from the 28 ground tracks identified by dark lines in Figure 1. The mean change in the height variance, averaged for all points along the 28 tracks, was used to gauge the effectiveness of each correction, as suggested by *Campbell* [1988]. Corrections were applied if they reduced the variance in the residual height by more than the point-to-point along-track variance, 9×10^{-4} m^2, which is an estimate of the instrument precision [*Chelton et al.*, 1990]. The results, summarized in Table 1, indicate that only the ocean tide, dry troposphere, and inverted barometer corrections met this criterion. By a small margin, the ECMWF dry troposphere correction was more effective than the FNOC correction. The electromagnetic (EM) bias correction significantly increases the variance and is apparently ineffective. In comparison, for the less variable northeast Pacific, *Campbell* [1988] applied just one correction, concluding that only the ocean tide consistently reduced the data variance.

Reconstructing Mean Sea Surface Height

Although the mean is removed from the measured SSH, it is nonetheless a dynamically important quantity. *Kelly and Gille* [1990] outlined a technique which permits reconstruction of the mean SSH from the variability of a meandering jet. The technique, which has subsequently been refined and applied by *Kelly* [1991], *Qiu et al.* [1991], and *Qiu* [1992], uses the basic assumption that a velocity jet has a Gaussian structure. In the case of the ACC, measurements in the Drake Passage suggest that the SAF and PF may be treated as separate Gaussian jets [*e.g. Peterson et al.*, 1982], as shown in Figure 3. (The CWB and any additional ACC fronts are estimated to be too far south to be consistently identified by the altimeter.) Using the geostrophic relation, the velocity is integrated to produce a SSH section which is an error function for each front:

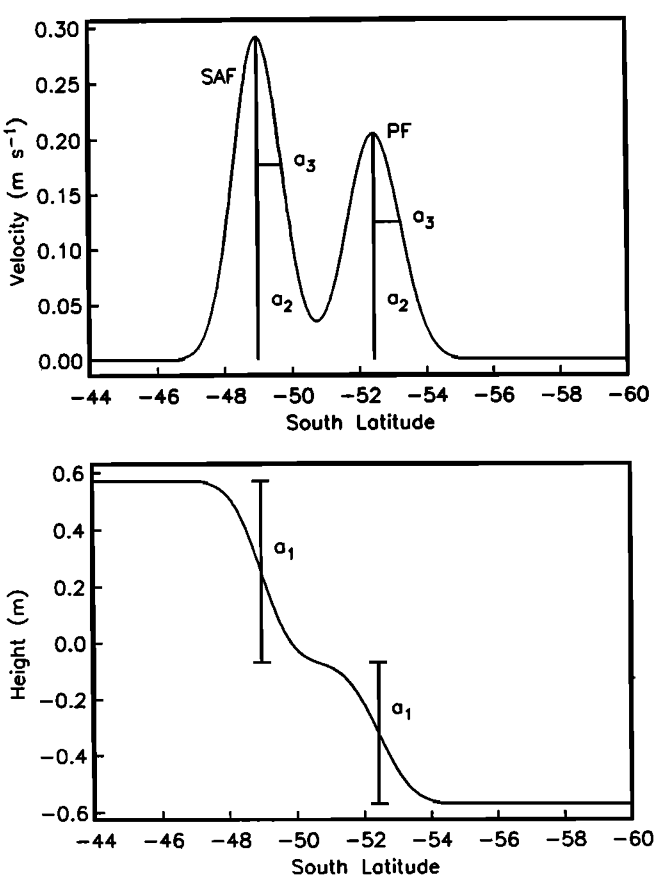

Figure 3. Schematic showing parameters defining sea surface height (SSH) error function.

$$
\begin{aligned}
h(x,t) &= \int_{a_2}^{x} \frac{a_1}{\sqrt{2\pi}a_3} \exp\left(-\frac{(x'-a_2)^2}{2a_3^2}\right) dx' \\
&= \frac{a_1}{2} \operatorname{erf}\left(\frac{x-a_2}{\sqrt{2}a_3}\right)
\end{aligned}
\qquad (1)
$$

centered at a_2, with width a_3, and total height change across the jet a_1.

Strong residual velocity features (or bumps in the residual height) are used to estimate error function parameters for the height a_1, location a_2, and width a_3, of the jet at the time of each satellite pass. Modeled heights for each satellite repeat are averaged to estimate mean height along the satellite ground track, which is added to the residual height data. Using a nonlinear fitting scheme (outlined below), the parameters of the error function are iteratively improved to provide better estimates of the true SSH. By repeating the sequence (constructing height profiles from parameters, averaging them to estimate the mean, adding the mean to residual data, and refitting the parameters), the mean height field estimate is fine tuned to best represent the data. In the right panel of Figure 2, the reconstructed mean plus residual height (solid line) contains substantial eddy variability, while the instantaneous fit (dashed line) smoothly captures the principle jet structure of the ACC.

The success of this approach is contingent on several key criteria. First, the residual height bumps corresponding to the jet must be large enough to be detected by the altimeter. Second, the jet studied should have a roughly Gaussian velocity structure. Third, it must meander substantially; *Qiu* [1992] found that the standard deviation of the position parameter, σ_{a_2}, should be at least twice the mean width parameter, $\overline{a_3}$, if a reliable estimate of the mean height field is to be obtained. Simulations conducted for the present study indicate that this criterion may be relaxed if the amplitude and width fluctuate along with the jet position. In the Kuroshio and in the Gulf Stream, these criteria are normally fulfilled. The strong single jets corresponding to 1-m height jumps are easily identified, and plausible height fields are produced, as confirmed by acoustic Doppler current profiler data [*Kelly et al.*, 1991] and by inverted echo sounder thermocline depth fluctuations [*Kelly and Watts*, 1994].

The ACC is potentially more difficult to study than the northern hemisphere western boundary currents because of its multiple jet structure and smaller associated sea surface topography fluctuations. The height jump across each of the ACC fronts is about 0.5 m [*Gordon et al.*, 1978] (henceforth GMB78), compared with 1 m for the Gulf Stream. Even so, the criteria required for a reliable reconstruction of the height field are nearly always satisfied. Residual height jumps along the ACC axes are large enough to be detected by the altimeter. The error analysis in section 3 indicates that the mean height is successfully reconstructed to within about a 10% error, without significant systematic bias.

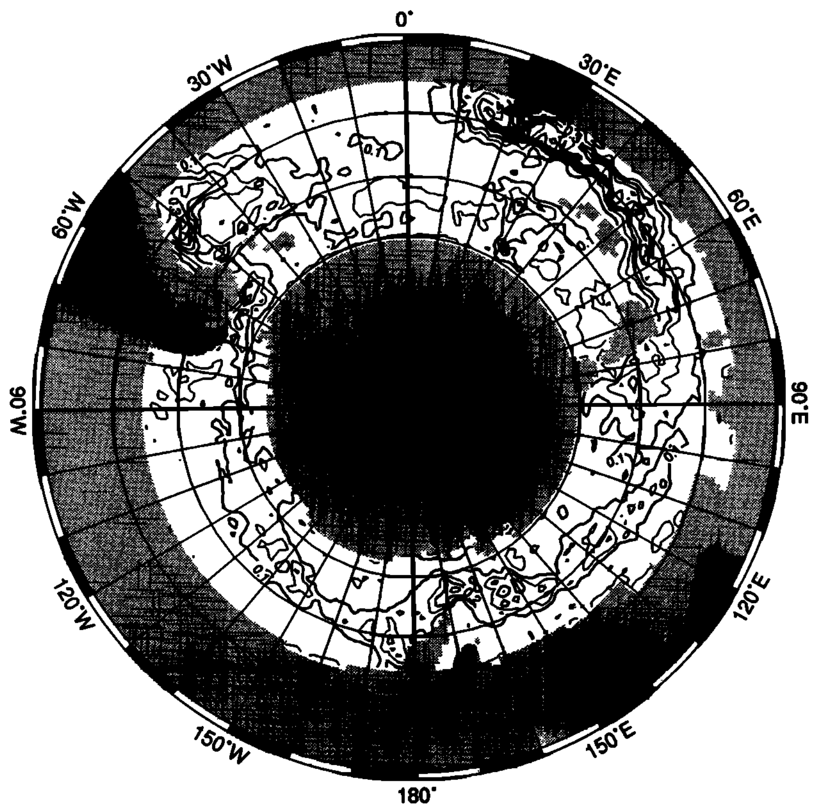

Figure 4. Root mean squared SSH variability (in meters) estimated from altimeter data and objective mapped using the same decorrelation function as for the mean SSH (discussed in section 4). Gray areas indicate regions where the error estimate exceeds 0.07 m or where no data is available.

Automation

Previous work using the error function model for instantaneous SSH has used largely interactive techniques to tweak parameters until a satisfactory fit is achieved. Because of the large quantity of data available for the Southern Ocean and the necessity of performing statistical tests on the data to assess the magnitude of the errors, for this study the data processing has been entirely automated.

First, initial guesses are obtained for the six parameters, a_i, representing position, width, and height of the SAF and PF as a function of time along each ground track. The appendix shows that the standard deviation of the SSH (shown in Figure 4) may be rescaled to serve as a reasonable proxy for mean geostrophic velocity; in turn, this is used to derive a first guess of the velocity field. Using the variance maxima (chosen to be within about 5° of the historic frontal locations) as rough constraints on mean jet positions, two velocity maxima are automatically selected to represent the SAF and the PF, and the corresponding jet parameters are identified.

These initial parameter guesses were iteratively improved by alternating application of the Levenberg-Marquardt procedure, a nonlinear least squares fitting algorithm [*Press et al.*, 1986] with automatic selection of new parameters based on the revised SSH estimates. By locally linearizing, the Levenberg-Marquardt scheme determines an optimal direction in parameter space to readjust the a_i in order to minimize the merit function:

$$\chi^2(t) = \sum_x \left[h'(x,t) + \overline{h}(x) - h_{\text{model}}(x, a_i, d)\right]^2, \quad (2)$$

where h' is again the measured residual SSH, $\overline{h}$ is the reconstructed mean SSH, and h_{model} is the instantaneous SSH. The value d is a constant offset which accounts for the residual orbit error and has no dynamical significance. The time variable, t, represents the satellite pass and has a maximum, N, which varies between 35 and 60. To improve the stability of the fitting process, the standard merit function, χ^2, was slightly modified to loosely anchor the parameters:

$$\tilde{\chi}^2(t) = \chi^2(t) + \sum_{i=1}^{6} \{b_i \cosh\left[c(a_i(t) - \overline{a}_i)\right]\}^2, \quad (3)$$

where b_i and c may be arbitrarily fixed to keep the parameters, $a_i(t)$ within a physically plausible range of $\overline{a}_i$. The hyperbolic cosine function is selected because it has little effect on a parameter a_i if it is near $\overline{a}_i$, but very dramatically changes a_i if it strays out of range. Between applications of the Levenberg-Marquardt technique, the parameters are reestimated by adding the revised mean SSH to the residual heights and selecting features corresponding to large SSH differences. The underlying assumption in estimating jet parameters is that the location of the jet is the critical parameter: if the correct bump in the SSH can be identified, then more precise estimates of the location, width, and height difference may be found by tuning. Residual bumps and dips in the SSH are interpreted as rings. Conditions for temporal and between track continuity are not included in the model; long-period, large-scale structure in the final results is therefore a rough indication of the overall consistency of this method. In locations where a third ACC front exists at a detectable latitude, the analysis may occasionally misidentify it as either the SAF or PF, though this does not appear to be a severe problem: in about 98% of adjacent track pairs, the mean is consistent with the presence of two continuous jets, though in some locations the jets may nearly merge.

3. Error Estimation

In order to estimate the error in the reconstructed mean SSH, Monte Carlo simulation was performed for the 28 tracks identified in Figure 1. (*Press et al.* [1986] outline the basic principles underlying this method.) Since both the accuracy (or bias) and the precision (or repeatability) of the nonlinear fitting are of concern, two different Monte Carlo schemes were developed. Both types of Monte Carlo simulation share common procedures: Begin with a 34-month time series of up to $N = 62$ SSH profiles along one of the ground tracks; estimate a time series of $7 \times N$ jet parameters and a mean SSH for the data; now add random noise to the original data to create multiple new data sets. (Ten to twenty sets of data with random noise were sufficient to produce error bars accurate to at least one significant digit.) Process each of these new data sets like the original data set to generate new estimates of the mean SSH and the $7 \times N$ parameters. Then compute the differences between the results from the original data and from the noise-added data to estimate error bars for the mean and for each of the parameters.

Assessing Bias From "Perfect" Data

How successfully did the nonlinear fitting procedure reconstruct a known mean with perfect data? To determine if there is a measurable bias in the procedures, a time series of six estimated parameters that define the instantaneous SSH was used to create a noiseless artificial data set from which the mean SSH was removed to produce "perfect" residual heights. Since the correct parameters are known, any systematic differences between the correct answers and simulated results will represent potential biases in the results. The resulting mean bias of 0.02 m was small compared with its standard deviation of 0.06 m.

In real data, eddies and rings along with instrument noise will lead to additional random error in the estimated mean height. To investigate the relative magnitudes of the bias compared with the error due to mesoscale noise, Monte Carlo simulations were performed by first adding noise to the synthetic data. The misfit between the modeled SSH and the reconstructed mean plus residual height is characteristic of large eddy features which occur near the SAF and PF. (In Figure 2, this misfit is the difference between the dashed and solid lines.) The spectrum of this difference was used to set the amplitude of random noise, with a minimum level of 0.03 m corresponding to the background noise of the Geosat altimeter. The noise spectrum with random phases was inverted to the spatial domain and low-pass filtered in the same way as the data. The addition of eddies did not substantially change the results of the no-eddy case: the mean bias, 0.03 m, was small compared with the standard deviation.

Assessing Repeatability (Precision)

Precision, or repeatability, is another measure of the success of a fitting scheme. To test precision, a second type of Monte Carlo procedure was employed by perturbing the original raw data with noise designed to best represent two types of measurement errors. Random white noise with about 0.03 m amplitude was combined with noise computed from the spectrum of the unused data corrections for the solid earth tide, ionospheric and wet tropospheric delays, and the EM bias, as shown in Figure 5. The EM bias correction, which dominated the spectrum, was red, with amplitudes of 0.1 to 0.2 m for long wavelengths, and a 0.03 m minimum amplitude was imposed. (The long-wave amplitudes of this spectrum are also large enough to account for *Chelton*'s [1988] estimated errors in the corrections applied to the data.) Noise generated by inverse Fourier transforming the amplitude with random phase was added to the raw

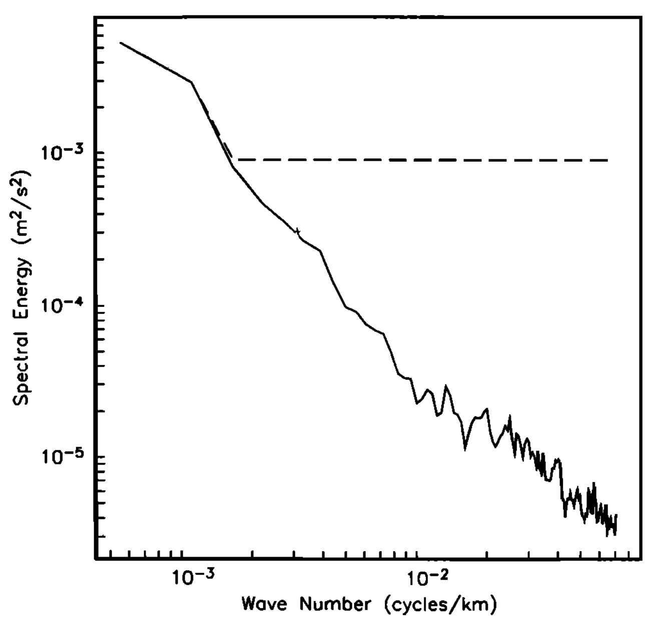

Figure 5. Spectrum of data corrections (solid line) for track d001. For the Monte Carlo simulations, a 0.03 m minimum level of white noise is added (dashed line.)

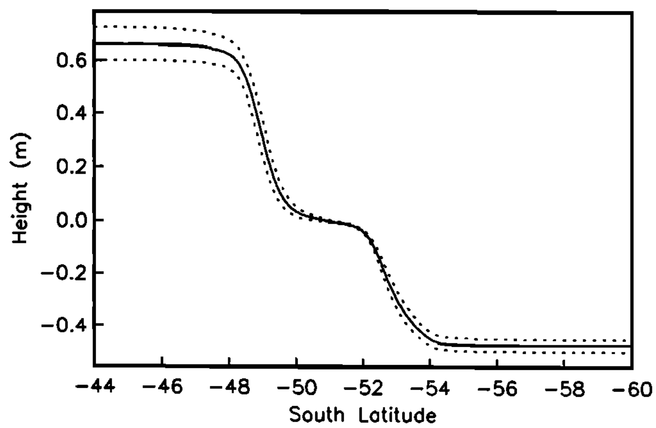

Figure 6. Mean SSH for track d001 (solid) and 1-σ RMS errors (dashed) estimated from Monte Carlo simulation. The error is smallest at the center because the separation between the jets is used as a fixed reference point.

data, and the resulting data were processed following the procedure outlined in section 2.

The mean root mean square (RMS) difference for all 28 ground tracks tested was 0.077 m, which represents about a 12% error in the mean SSH. Figure 6 shows the reconstructed mean SSH for one sample track, d001, along with the RMS error computed based on 20 simulations with noisy data. The RMS error and the reciprocal square root of the number of cycles, $N^{-\frac{1}{2}}$, have a correlation coefficient of 0.48, which exceeds the 95% significance level. A linear regression of this relationship was used to estimate the SSH error for ground tracks where Monte Carlo simulations were not performed.

Errors were also computed for each of the six jet parameters. (The constant offset is considered arbitrary.) They are listed in Table 2. All of the distributions are centered at zero, indicating no substantial bias in the parameters, but the distributions have long tails; thus a double exponential probability distribution may be more appropriate than the usual Gaussian normal distribution to characterize errors in the parameters, and statistically robust techniques should be employed to interpret these parameters. Therefore the mean absolute value of the error (the L1 norm) rather than the standard deviation was used for some analyses. Table 2 also shows that the error estimates computed from the diagonals of the linearized covariance matrix for the Levenberg-Marquardt nonlinear fit are in most cases about the same order of magnitude as the error bars from the Monte Carlo simulation, but occasionally the nonlinear fit generates excessively large error estimates. The mean Monte Carlo simulation results, presented at the end of Table 2, provide a more consistently reliable error estimate.

Based on the Monte Carlo simulation results, the signal-to-noise ratio appears large enough to permit consideration of time-dependent characteristics of the ACC frontal structure. Figure 7 shows a time series for one subtrack of the total height difference across the combined SAF and PF along with RMS errors at each point. While the error bars are occasionally quite large, low-frequency fluctuations have an amplitude of about 0.15 m, which is significantly greater than most

Table 2. Mean Values and Results of Monte Carlo Simulation for Gaussian Jet Parameters for SAF and PF for Four Tracks

Parameter	Mean Absolute Value of Error	Error From Covariance Matrix	Mean Value
	Track a000		
SAF			
a_1 height	0.13	0.15	0.42
a_2 position	0.88	0.49	-48.73
a_3 width	0.25	0.26	0.42
PF			
a_1 height	0.15	0.17	0.72
a_2 position	0.24	2.08	-50.67
a_3 width	0.16	0.09	0.42
	Track a008		
SAF			
a_1 height	0.12	0.16	0.81
a_2 position	0.17	0.19	-52.73
a_3 width	0.12	0.08	0.54
PF			
a_1 height	0.11	0.17	0.78
a_2 position	0.66	0.26	-55.47
a_3 width	0.23	0.21	0.31
	Track d000		
SAF			
a_1 height	0.33	0.21	0.71
a_2 position	0.84	8.96	-55.40
a_3 width	0.25	14.12	0.27
PF			
a_1 height	0.32	0.25	0.78
a_2 position	0.72	1.41	-56.98
a_3 width	0.26	0.62	0.30
	Track d008		
SAF			
a_1 height	0.17	0.19	0.62
a_2 position	0.38	0.88	-43.05
a_3 width	0.26	0.14	0.56
PF			
a_1 height	0.15	0.17	0.78
a_2 position	0.36	0.60	-44.97
a_3 width	0.19	0.25	0.46
	Mean		
SAF			
a_1 height	0.17	0.18	0.68
a_2 position	0.54	4.16	-49.76
a_3 width	0.17	1.06	0.40
PF			
a_1 height	0.15	0.19	0.60
a_2 position	0.53	0.69	-53.04
a_3 width	0.17	0.33	0.39

The mean absolute value of the error (the L1 norm) is shown along with the error estimated based on the covariance matrix computed for the Levenberg-Marquardt fit and the mean values of each of the parameters. Here, a_1 heights are in meters; a_2 positions and a_3 widths are in degrees latitude.

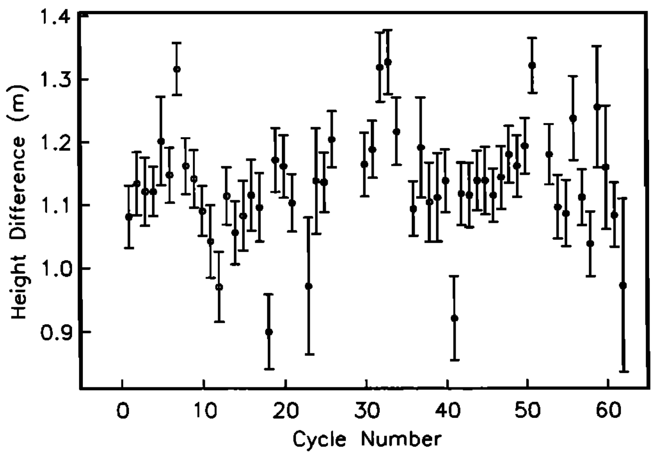

Figure 7. Time series of total height difference across the SAF and PF, with (L1 norm) error computed based on 20 Monte Carlo simulations for track d001.

of the estimated error bars. The standard deviation of time-dependent fluctuations throughout the Southern Ocean, 7% of the mean, is comparable to the 8% fluctuations in total transport observed by *Whitworth and Peterson* [1985] in Drake Passage. In their transport data record, as in the height results presented here, the maximum amplitude of the fluctuations is 16% of the mean, suggesting that the magnitude of variability observed in Drake Passage may be representative of the entire circumpolar system. Future work with the altimeter-derived mean SSH data will examine the time dependence and the dynamics controlling the ACC in greater detail, but the remainder of this paper focuses on the mean ACC.

4. Mapping Regional Results

Mean Sea Surface Height

Mean heights were estimated for all of the track segments shown in Figure 1 and were objective mapped using the method outlined by *Bretherton et al.* [1976]. Covariance functions needed to objective map the height fields were obtained by least squares fitting of data covariances to a function of the form

$$c_{i,j} = A \exp\left[-\left(\frac{\Delta x_{ij}^2}{B_1^2} + \frac{\Delta y_{ij}^2}{B_2^2}\right)\right] + C_1\delta_{ij} + C_2\delta_{kl} \quad (4)$$

where A is the amplitude corresponding to the zero-lag covariance. Because the data variance depends strongly on whether a point is within or outside a jet, A is largest where the variance is largest, along the core of the ACC, and attenuates with distance from the jets according to the empirical relation:

$$A = 0.1 \exp\left(-\frac{\Delta y^2}{(1.8^\circ)^2}\right) + 0.02 \text{ m}^2 \quad (5)$$

where Δy is the difference in degrees latitude between the SAF–PF midpoint and the objective map grid point. B_1 and B_2 are zonal and meridional decorrelation length scales. Using adjacent ground tracks, the zonal scale, B_1, was estimated to be about 200 km. The along-track length scale is about 160 km. Combining this information with the zonal length scales to project into the meridional direction, the meridional length scale, B_2, is estimated to be 100 km. These distances are less than half of the 450-km zonal and 350-km meridional length scales used by *Olbers et al.* [1992] for objective mapping temporally and spatially coarser hydrographic data and indicate that the maps produced from altimeter data should retain greater spatial structure. C_1 and C_2 represent the error variance, and the subscripts i and j refer to individual data points (regardless of subtrack), while the subscripts k and l refer to different satellite ground tracks. The quantity $C_1 + C_2$ is estimated from the data to be approximately 0.012 m^2. The value of C_2 estimated from the Monte Carlo simulation is $(7.7 \times 10^{-4}$ m$)^2$ or about 60×10^{-4} m^2. Thus C_1 is also set to 60×10^{-4} m^2. Note that C_2 is nonzero because errors in the mean are correlated from point to point along the satellite subtracks though not between satellite tracks. C_1 accounts for the uncorrelated error at each measurement point.

To eliminate residual orbit error between different ground tracks, heights along each ground track are adjusted by an additive constant, which is determined by minimizing ascending and descending track crossover differences in a least squares sense; this constant is typically smaller than 0.1 m. The resulting mean SSH field, mapped with 1° resolution, is shown in Plate 1.

5. Discussion

The mean SSH based on the altimeter data (Plate 1) shows that the height gradient associated with the ACC occurs in a relatively narrow region. This clearly contrasts with the broader flow patterns indicated by dynamic topography computed from *Olbers et al.*'s [1992] gridded data (Figure 8). No sharp position changes between adjacent tracks or localized error increases exist to suggest discontinuities in the ACC. Although the two jets are not clearly discernible in Plate 1 because of the large geographic domain shown and coarse 1° gridding of the map, the ACC is consistently modeled as two sharp eastward jets throughout the Southern Ocean.

Jet Statistics

The Gaussian model parameters provide a simple means to characterize the structure of the ACC jets and to track changes in the ACC. Mean parameter values are summarized in Table 2. In Figure 9, the mean latitudes of the SAF and PF, objectively mapped using data from ascending and descending tracks, indicate that the jets are closely steered by bathymetry, in agreement with analyses of hydrographic data [GMB78]. The

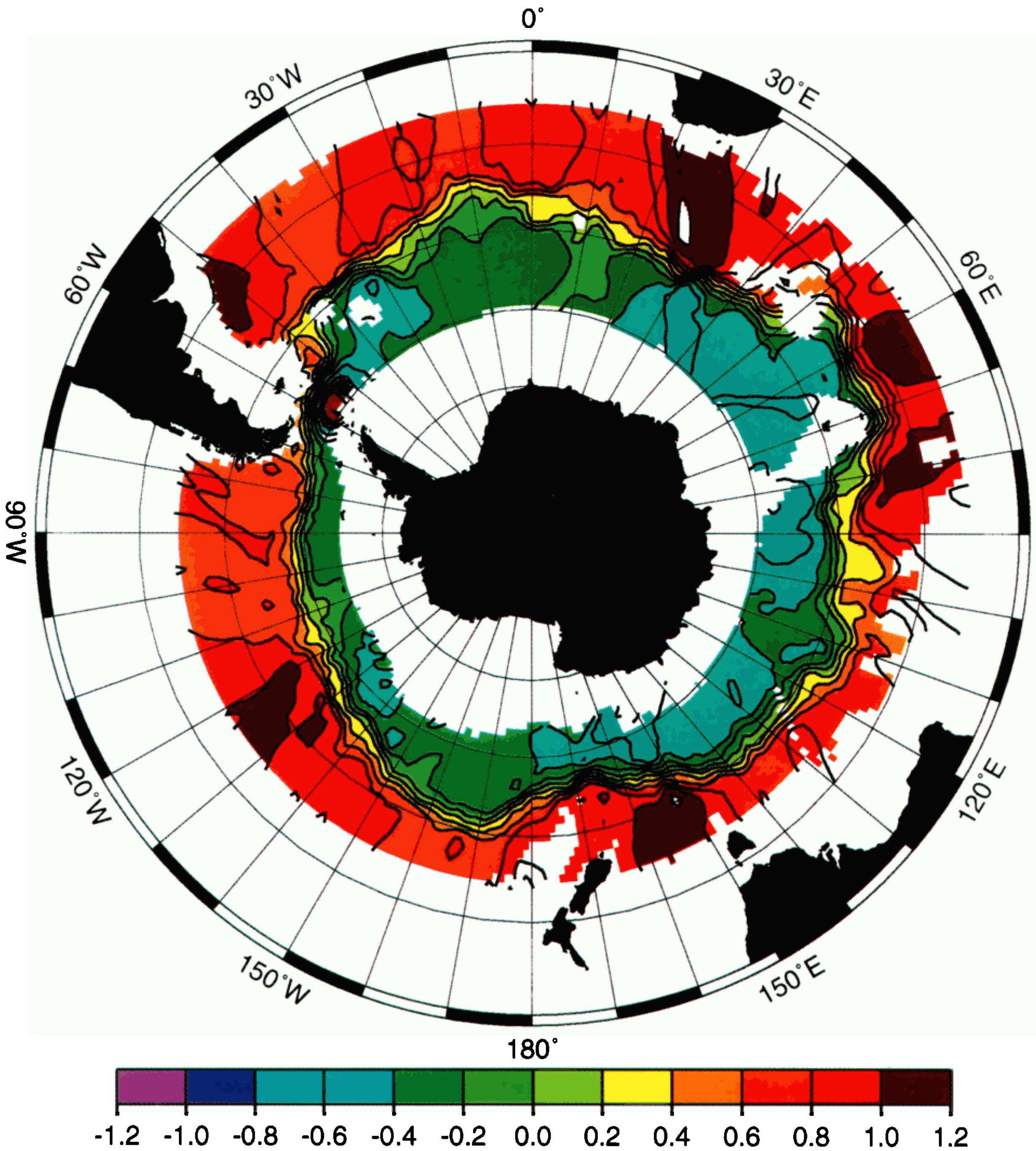

Plate 1. Objective mapped reconstructed mean SSH, contoured at 0.2-m intervals. The 0-m height contour separates the SAF (positive heights) from the PF (negative heights). Regions with no data or height errors greater than 0.05 m are white, and contours are not shown when the error exceeds 0.1 m. Typical errors are between 0.04 and 0.05 m.

response of the SAF and PF to specific topographic features, such as the Eltanin and Udintsev Fracture Zones around 130°W, will be discussed in the geographic tour of the Southern Ocean later in this section. The meridional separation between the fronts varies from 55 km to 900 km, with a mean separation of 310 km. Over time both jets meander; however, the mean absolute value of the position fluctuations (the L1 norm) is 0.47°, which is less than the error estimates from Table 2 (0.54° and 0.53°), indicating that the signal-to-noise ratio is small and detailed information about the global time series may be difficult to extract.

The mean height difference across the two fronts is 1.3 m. This is slightly larger than the 1.1 m dynamic height difference found by referencing historic data to 2500 or 3000 m [*Gordon et al.*, 1982; *Olbers et al.*, 1992]. Figure 10 shows how the mean height difference varies around the Southern Ocean. Though the total

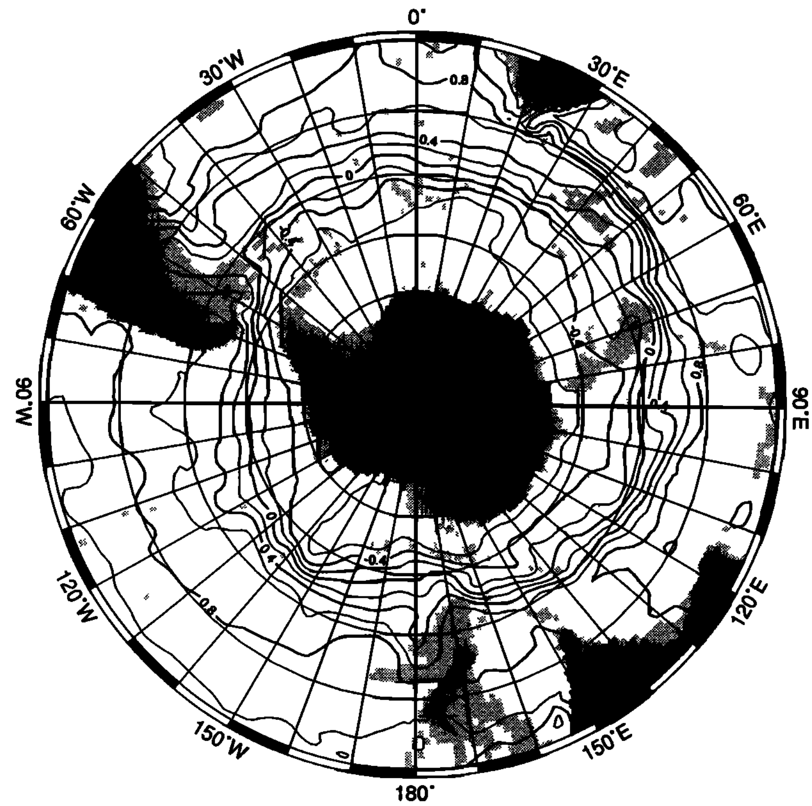

Figure 8. Historic mean dynamic height (in meters) from *Olbers et al* [1992]. Dynamic topography is referenced to 2500 m, and has been adjusted by an arbitrary constant to simplify comparison with the reconstructed SSH shown in Plate 1.

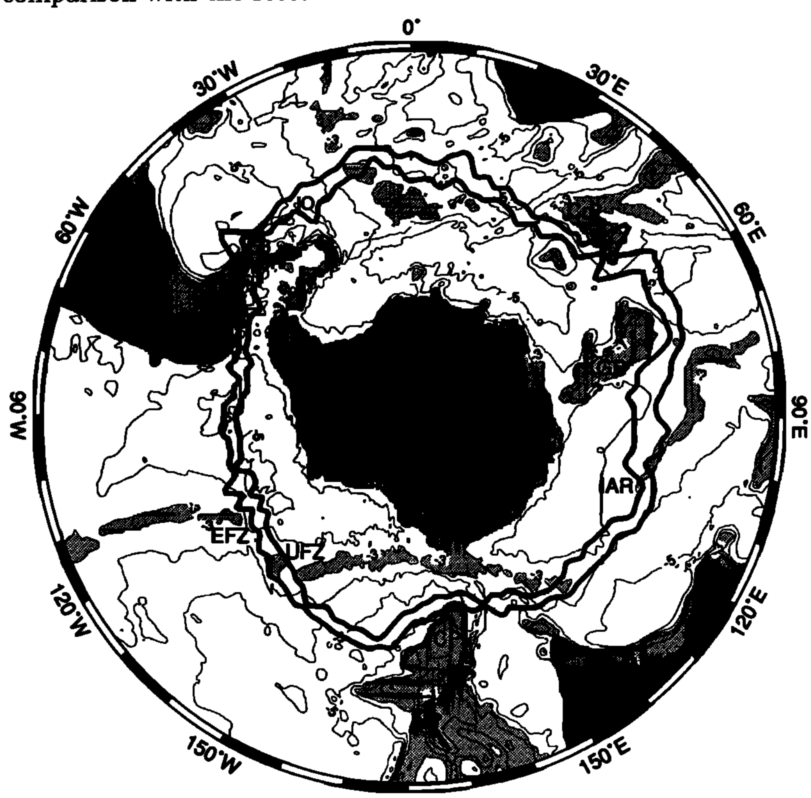

Figure 9. Bathymetry in kilometers from gridded 5 minute data smoothed over 100 km lengthscales. Regions shallower than 3 km are shaded gray. Indicated features are Indian-Antarctic Ridge (IAR), Campbell Plateau (CP), Udintsev Fracture Zone (UFZ), Eltanin Fracture Zone (EFZ), Scotia Ridge (SR), Ewing Bank (EB), Islas Orcadas Rise (IO), Crozet Plateau (CrP), Kerguelen-Gaussberg Plateau (KGP). The heavy shallow lines represent the mean paths of the SAF and PF.

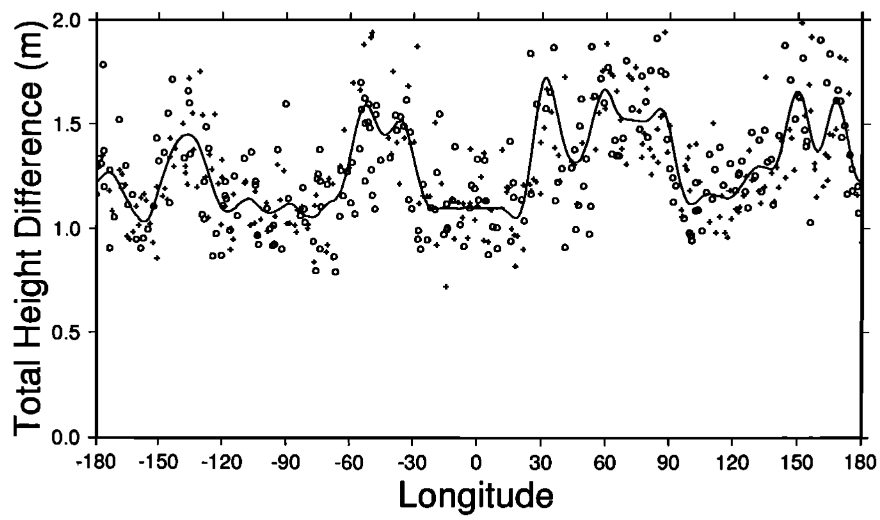

Figure 10. Mean height across both the SAF and PF as a function of longitude for ascending tracks (circles) and descending tracks (pluses). The solid line represents the objectively mapped height differences.

height difference shows substantial scatter, consistent with the error estimates in Table 2, one striking feature is its apparent tendency to oscillate between two values, a minimum around 1.1 m and a larger value around 1.5 m. The 1.1-m difference may represent the circumpolar flow, and the larger height differences correspond to regions where, for example, parts of the recirculating subtropical gyre in the Indian Ocean (between 20° and 80°E) or the Weddell Sea gyre (between 70° and 40°W) join the circumpolar flow. The height differences across the jets are correlated with the SSH variance with a coefficient of 0.60, which is significant at the 99.9% level. Simulations using artificial data indicate that this correlation is not an artifact of the data processing. Maps by *Johnson et al.* [1992] and *Morrow et al.* [1992] suggest that regions of high height variance are associated with increased Reynolds stress terms; therefore changes in the height differences may be linked to changes in the importance of the ageostrophic components of the momentum balance rather than to changes in transport.

Figure 11 shows histograms of all heights within the Southern Ocean. The most common heights represent the relatively flat regions outside of the ACC. The strong height gradients across the ACC jets correspond to less frequently occurring heights. The dynamic height from *Olbers et al.*'s [1992] gridded atlas data (Figure 11a) does not distinguish two separate ACC jets because the probability decreases gradually near zero, the height value separating the jets. The distribution of mean SSH for all the satellite tracks with no crossover corrections added (Figure 11b) suggests two distinct jets separated by the zero height contour. The addition of a crossover correction (Figure 11c) tends to blur the distinction between the fronts and suggests that the height contour separating the SAF and the PF may vary geographically from the nominal zero value.

The mean value for the width parameter, a_3, for both the SAF and the PF is 0.40° latitude (54 km in the along-track direction or 44 km in the meridional direction). Since the standard deviations of the jet positions are substantially larger than their widths (Table 2), the mean should be reconstructed without significant bias, based on *Qiu*'s [1992] tests and the Monte Carlo error simulations.

The spatial variations of the frontal widths are plotted in Figure 12. Although the along-track width differs substantially between adjacent tracks, Figure 12 suggests that the widths of the fronts vary by about 20% over large spatial scales. Variations in the mean angle at which the satellite groundtracks intersect the fronts cannot explain this trend.

Two factors should control the width of the ACC jets. First, the baroclinic Rossby radius, L_r, defines a horizontal length-scale for stable mesoscale features. For an ocean of depth D and constant Brunt-Väisälä frequency, N, L_r is ND/f. Estimates of L_r using varying N from *Olbers et al.*'s [1992] gridded data indicate that the dominant variation in L_r is because of fluctuations in f. Thus, as the latitudes of the SAF and PF change around the Southern Ocean, stability constraints require that the widths of the fronts adjust with $1/f$. As the fronts flow southward from the dateline to Drake Passage (around 80°W), both narrow gradually. Beyond Drake Passage, they move northward through the Scotia Ridge and broaden abruptly; the SAF is widest around 10°E and the PF widest around 60°E, where it is also furthest north. Both fronts narrow and move southward as they continue eastward to the dateline. The correlation coefficient for width and $1/f$ (Figure 13) is 0.53 for the SAF and 0.51 for the PF; both are statistically significant at the 99.9% level, and a chi-squared test for the linear regression yields a value of 0.9, indicating a reasonable match between the estimated error bars and the statistical deviation. The

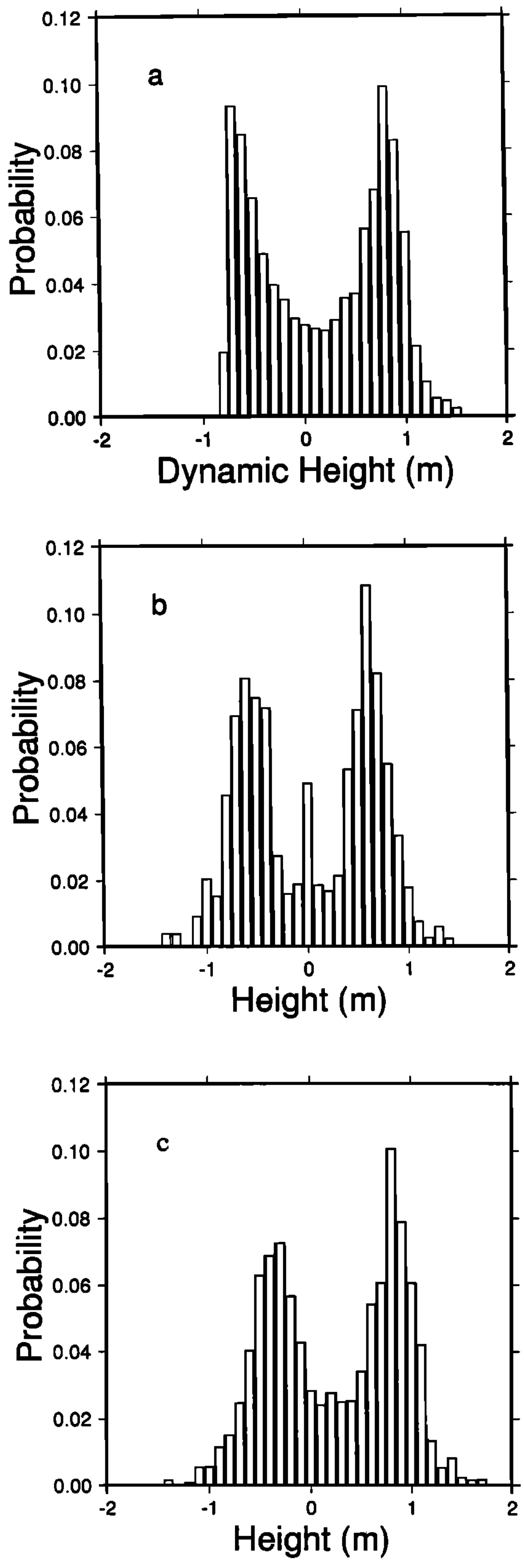

Figure 11. Histograms showing distribution of (a) dynamic topography in meters (from *Olbers et al.* [1992]'s gridded atlas data), (b) mean SSH derived from Geosat data, and (c) mean SSH from Geosat data with crossover correction to correspond to the SSH in Plate 1. In these histograms, the zero-height line is adjusted to fall between the SAF and the PF.

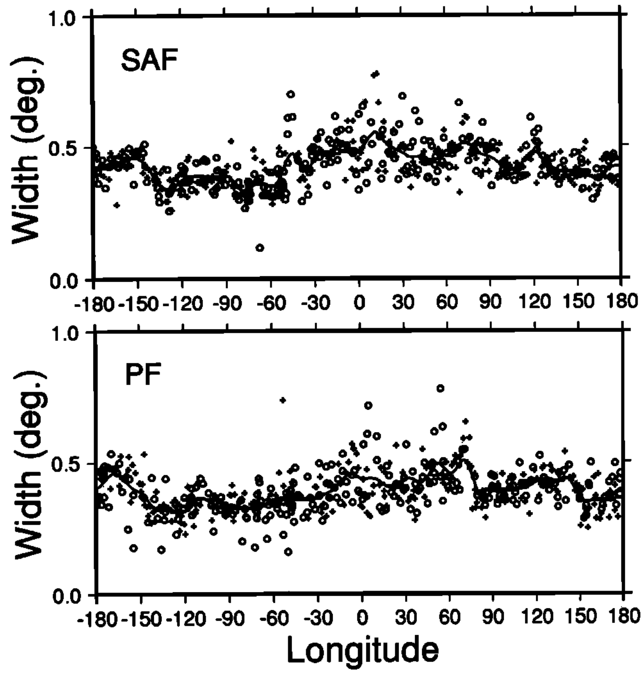

Figure 12. Mean width of the SAF (top) and PF (bottom) as a function of longitude. Values for ascending tracks are shown as circles; descending widths are shown as pluses signs. Solid lines are determined by objectively mapping the widths.

correlation coefficient between L_r and the width (both of which are relatively noisy) is smaller, 0.25 for the two fronts combined, but still statistically significant at the 99% level. *Stammer and Böning* [1992] found a similar relationship between L_r and characteristic eddy length scales determined from autocovariance functions for Geosat data.

The second factor controlling the width is conservation of the total ACC transport. Since the geostrophic surface velocity of the jet is

$$u_s \sim \frac{ga_1}{fa_3}, \tag{6}$$

the surface transport is

$$T_s \sim \frac{ga_1}{|f|}, \tag{7}$$

and the total transport is

$$T \sim \frac{ga_1\Phi}{|f|}, \tag{8}$$

where Φ represents the attenuation of the velocity with depth and may be interpreted as an equivalent depth. Although a_1 fluctuates (Figure 10), it does not vary systematically with latitude. Since the width, a_3, is proportional to $1/|f|$, then $u_s \sim ga_1$, and surface transport varies with $1/|f|$. Estimates of the vertical velocity structure of the ACC from *Olbers et al.*'s [1992] data suggest that Φ varies with $|f|$. Therefore transport varies with SSH difference, $T \sim ga_1$. In locations

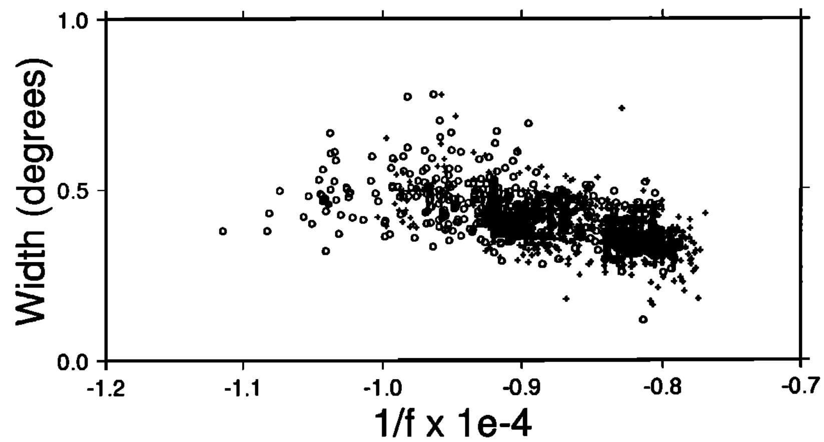

Figure 13. Width of the SAF (circles) and PF (pluses) versus the reciprocal of $|f|$.

where the SAF and PF move southward ($|f|$ increases), baroclinic processes may act to deepen the flow (Φ increases) in order to conserve transport. The augmented eddy activity near topographic features which steer the ACC, indicated in Figure 4, suggests active instability processes may be adjusting the vertical structure.

Height Variance

The variance of the SSH measured by the altimeter (Figure 4) is greatest along the central axes of the ACC. In this core region between 40% and 70% of the height variance is explained by the Gaussian model for the meandering (Figure 14). The remaining variance represents rings and eddies separate from the jets, as well as the meandering mean flow in regions of the Southern Ocean that are not included in this model such as the Falkland Current and the Agulhas Retroflection. The percentage of height variance accounted for by the reconstructed mean is smaller in regions of increased eddy activity, which *Chelton et al.* [1990] noted are associated with large topographic features such as the ridge downstream of Drake Passage or the Crozet

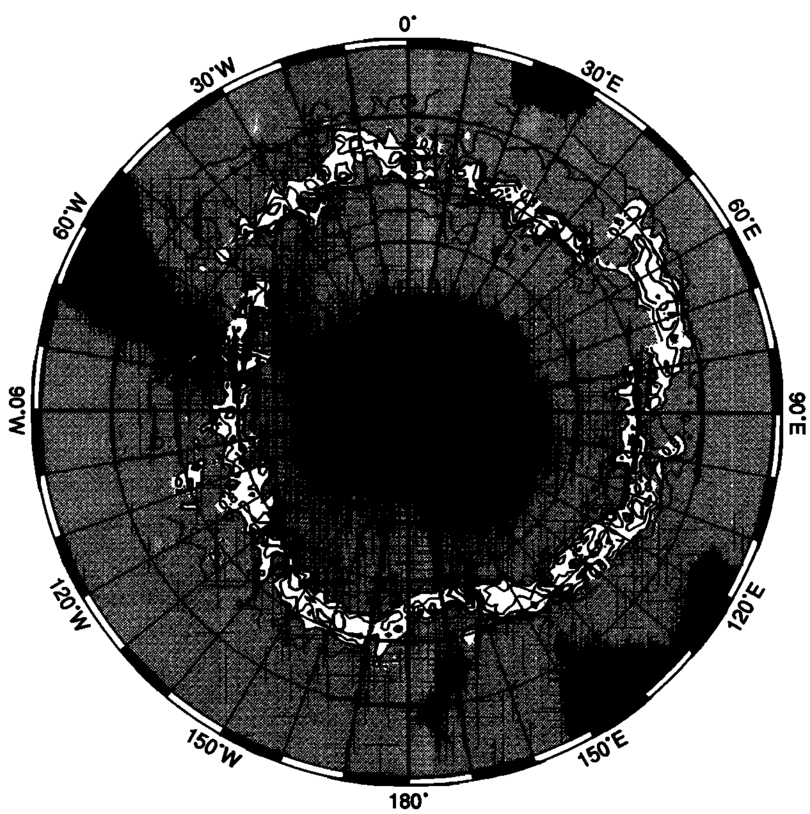

Figure 14. Ratio of root mean squared SSH residual variability, after modeled effects of SAF and PF have been removed, to root mean squared variability of the altimeter-measured height field. Gray areas indicate locations where no data are available or where less than 20% of the variance is explained by the meandering jet model.

Plateau area. This suggests that topographic features may cause ring formation rather than increased jet meandering.

Mean Mapped Sea Surface Height

A few words of explanation will help the reader better interpret the mean height in Plate 1. The error function model used to reconstruct mean SSH applies only to the jets themselves but includes no recirculation and no large-scale structure. Thus the mean height depicted in this map should be accurate within the limits of its error bars for mesoscale variations in the jet but cannot capture basin scale height variations. For example, this model cannot verify whether the south Pacific Ocean is 0.38 m higher than the south Atlantic, as suggested by *Reid* [1961]. In addition, height contours which leave the mean axis in the map could identify water entering the ACC from outside the mapped region, but they could also signal ageostrophic phenomena or the effects of a recirculating flow within the mapped domain.

Several factors account for the differences between the historic picture of the ACC as a broad eastward flow and the altimetric view of a pair of narrow jets. The most likely source of differences stems from the finer resolution provided by the altimeter, which better resolves the ACC mean structure. Time-sampling considerations may also contribute to the differences. While the altimeter data represents a 30-month period in the late 1980s, the historic in situ data includes data from the 1940s through the 1980s, concentrated primarily during the *Eltanin* cruises of the late 1960s and early 1970s. Any substantial low-frequency shifts in ACC jet locations over the 40-year period might smear the mean ACC into a broad flow, and a local change in the structure of the ACC between the *Eltanin* period and the late 1980s could also account for qualitative differences in the height fields.

Finally, because the orbit corrections remove the basin scale signal, only narrow jets can be seen by the error function model. Thus if the flow were as broad as the historic data suggests and no jets existed, the algorithm could misinterpret rings or other mesoscale features as jets. However, since rings do not typically have the spatial and temporal coherence of jets, this seems unlikely to create substantial errors on the basin scale.

The following detailed examination of the altimeter mean SSH will highlight the major features of the ACC, emphasizing its response to specific bathymetric features and the differences between the altimeter picture of the ACC and the dynamic height from in situ data. The discussion follows the same organizational structure as GMB78's discussion of the Southern Ocean topography from historic data.

South of Australia, 100°— 140°E

South of Australia, the SAF and PF are on opposite sides of the zonal Indian-Antarctic Ridge, in qualitative agreement with hydrographic measurements. The altimeter data frequently indicate the presence of eddylike features situated between the SAF and the PF. Because of difficulties in the nonlinear fitting, the data are not sufficient to assess whether this variability might represent westward counterflow over the ridge, as suggested by *Callahan* [1971] or transient eddies, as GMB78's analysis and *Savchenko et al.*'s [1978] XBT survey indicated.

Tasman Sea-Campbell Plateau, 140°— 180°E

At 140°E, the PF crosses through a gap in the Indian-Antarctic Ridge to flow adjacent to the SAF on the northern side of the ridge. At this point, the height contours pinch together slightly as the jets are closer together. The ACC flows southward to move through openings in the Macquarie Ridge-Hjort Trench system around 160°E. In agreement with *Gordon*'s [1972] observations, the SAF flows through an opening at about 53°S, to the north of Macquarie Island; the PF passes just south of Macquarie Island but slightly north of the pathway identified by Gordon. Southeast of the ridge system, the two fronts converge slightly and move around Campbell Plateau south of New Zealand.

To the east of New Zealand, historic data indicates that the PF follows the northern flank of the Pacific-Antarctic ridge located at about 60°S, while the SAF presses against the Campbell Plateau. This analysis does not place the PF as far south but instead shows both fronts moving northward in parallel around Campbell Plateau. A loss in total SSH difference at about 175°W may be a sign that the actual PF is too far south to be resolved by the altimeter, though it could also indicate the action of another dynamical process.

Southwest Pacific, 180°— 130°W

At 170°W, the ACC turns eastward and moves across the abyssal plain. The PF crosses through the Udintsev Fracture Zone and the SAF crosses through the Eltanin Fracture Zone in the Pacific-Antarctic Ridge around 140°W. At this point, the height contours converge and increase in number, suggesting a narrow and intensified transport through the ridge system. The ACC paths through the ridge gaps are readily apparent in the hydrographic data and have been interpreted as a clear indication of the coupling between surface flow and deep topography [*Gordon*, 1967; GMB78].

Southeast Pacific, 130°— 80°W

East of the mid-ocean ridge, the altimeter data indicates narrow jets continuing southward toward Drake Passage, in contrast to the historic hydrographic data which shows the current rapidly broadening into a diffuse eastward flow without a clear axis [GMB78; *Reid*, 1986]. A slight reduction in the number of height contours across the fronts suggests that some of the transport may recirculate through the central Pacific and that the jets are less intense in the eastern Pacific than they are at the mid-Pacific ridge.

Drake Passage, 80°— 55°W

The narrow opening through Drake Passage at 70°W refocuses the ACC jets. In both the historic data and the altimeter data, the flow begins to move northeast, and the height contours converge, suggesting an intensified, higher velocity flow.

There is no evidence for the SAF turning north along the South American continental shelf and retroflecting when it meets the Brazil Current at 40°S [*Peterson and Whitworth*, 1989] (henceforth PW) because shallow water regions could not be analyzed, and the convoluted retroflecting SAF axis is not easily described by a double error function model. PW's estimate of the Falkland Current width, 150 km at 200 m depth, is comparable to the full width of the Gaussian SAF ($4a_3$), 175 km. They found the Falkland Current to be about 150 km wide at 200 m depth. A comparable measure of the width for the Gaussian jet model used in this analysis is 4 times the width parameter, a_3, for a total meridional width of 175 km at the surface.

Southwest Atlantic, 55°— 0°W

Between about 55° and 45°W, the SAF and PF move northward through the Scotia Ridge. Because of the difficulties in capturing the retroflecting Falkland Current, the altimeter analysis shows the SAF slightly east of the front location identified by PW, but the PF follows a trajectory very similar to the one indicated by their analysis of hydrographic data.

Once the SAF and PF cross through the Scotia Ridge, they flow along the northern edge of the Ewing Bank and the Falkland Ridge. To the north of the Ewing Bank, altimeter height contours pinch together tightly, appearing to form a single intense jet near 45°W. This is consistent with PW, who found that the SAF and PF are very close together at this longitude and may sometimes merge to form a single jet. Along the Falkland Ridge to about 30°W, the SAF and PF appear to be closely controlled by bathymetry in both altimetry and hydrography.

As the ACC flows eastward past the Islas Orcadas Rise, its path is less well defined and shows substantial meandering, which may mean that the flow is too weak and broad to be clearly identified by the automated nonlinear fitting code. The SAF and PF generally flow zonally across the Atlantic between 45° and 50°S. Hydrographic surveys of the central South Atlantic are limited, making verification of altimeter observations difficult, but dynamic topography maps [GMB78; *Reid*, 1989] indicate zonal flow.

Southeast Atlantic and the Southwest Indian Oceans, 0°— 40°E

The retroflecting Agulhas Current is the largest source of height variability in the southeastern Atlantic and southwestern Indian Oceans, but because it is not considered a circumpolar flow, it is not included in the reconstructed mean. The SAF and PF appear distinctly separate from the Agulhas, flowing eastward at 50°S, 10°–15°south of the retroflection region and the Crozet Plateau, consistent with hydrographic observations [*Jacobs and Georgi*, 1977; GMB78]. The SAF and PF are distinct features, though they converge at 33°E, where a hydrographic survey by *Read and Pollard* [1993] also found them merged together.

South Indian Ocean, 40°— 100°E

Between 40° and 50°E, the SAF and PF move abruptly northward in agreement with *Jacob and Georgi*'s [1977] STD sections. A deep passage in Crozet Plateau steers the SAF from its southern position at 40°E to the north side of the plateau, where *Park et al.* [1993] observed it. The PF moves northward east of Crozet Plateau. The SAF flows north of the Kerguelen-Gaussberg Plateau in both historic and altimeter data. The altimeter data indicate that the PF also takes a northward route around Kerguelen Island, but because the Gaussberg Plateau is too shallow for the tidal correction model, alternative paths to the south are not easily investigated. The hydrographic record does not offer a definitive map of the PF either; although the temperature indicator for the PF appears north of Kerguelen [*Park et al.*, 1991], *Park et al.* [1993] hypothesize that the PF follows a southerly route but loops northward immediately to the east of Kerguelen to flow parallel to the SAF.

Thus the two strong fronts north of Kerguelen could be the SAF and STF, which have been observed in close proximity or even merged into a single front [*Park et al.*, 1991]. Since altimeter data does not include thermohaline signatures and the height along each track is offset by a constant, this is difficult to verify. However, several contours which leave the ACC and enter the Indian Ocean, consistent with dynamic topography (Figure 8, GMB78, and *Park et al.*, [1991]), suggest that the STF is separating from the SAF to recirculate through the Indian Ocean.

Geographic Summary

Overall, the SSH from the altimeter data agrees qualitatively with historic hydrographic measurements but supports the idea that narrow jets exist around the entire Southern Ocean. The techniques developed here for reconstructing mean flow in the Southern Ocean are specifically adapted to maintaining mesoscale spatial structure and were designed to be robust with respect to the types of errors in Geosat data. Nonetheless, the technique is applicable for newer altimeter data from ERS-1 or TOPEX-POSEIDON. Though TOPEX's 64° turning latitude and coarser spatial resolution may pose difficulties for this type of investigation, the new satellite has better orbit tracking, and a more reliable large-scale geoid is now available, so that for basin scale analyses the mean SSH may be accessible, in addition to the variability. These improvements could permit the development of a better estimate of mean SSH by merging a mesoscale mean, derived using the techniques discussed in this paper, with large-scale measured SSH.

6. Summary

The ACC has been modeled as two meandering Gaussian jets. Using the height as a guide to the jet locations and intensity, the mesoscale height field across the ACC jets was iteratively reconstructed using a nonlinear fitting procedure. The technique was applied to all 244 ascending and 244 descending satellite tracks which cover the Southern Ocean. Each ground track was repeated every 17 days, providing between 30 and 60 sets of measurements during the 30-month Geosat Exact Repeat Mission. Error estimates obtained using two types of Monte Carlo simulation indicated a negligible bias and 0.077 m RMS error in the results. The resulting mean SSH was objective mapped with a meridional decorrelation distance of 100 km and a zonal decorrelation scale of 200 km.

The reconstructed along-track mean ACC height is consistent with the presence of two narrow circumpolar jets, which have an average separation of 310 km, although in a few locations they may merge to form a single jet. The jets meander about 1.7 times their width but less than the total average jet separation, so that the two jets are generally distinguishable in the mean field. The latitude of the ACC axes varies from 40° to 60°S, but the flow retains its sharp frontal structure all the way around its circumpolar trajectory. The substantial variations in latitude lead to variations in the baroclinic Rossby radius, and the widths of the SAF and PF adjust to match these changes in the Rossby radius. Estimates from hydrographic data suggest that the equivalent depth adjusts with latitude to make the transport proportional to the height difference across the jet. The flow is roughly steered by bathymetry. The jet model explains 40% to 70% of the altimeter height variance within the core of the ACC jets; in contrast to results from the Gulf Stream and the Kuroshio Extension, the percentage is smaller in regions of high variability, here associated with large topographic features. This points to the importance of eddy shedding and ring formation events in ACC dynamics.

Appendix: Height Variance and Mean Velocity

High variance regions are closely linked with regions of large mean velocity; using Geosat data, *Chelton et al.* [1990] showed that the standard deviation of SSH in the Southern Ocean and the mean geostrophic velocity from hydrographic data have a geographical correlation of 0.64. Despite the observational evidence, the connection between residual SSH and instantaneous SSH or mean surface velocity may not be intuitive. Here I develop a statistical framework to link the height variance to the mean jet velocity.

First, assume that the flow consists of a Gaussian jet which meanders about its mean position. Then the time-varying SSH may be written

$$h(x,t) = A\left[\operatorname{erf}\left(\frac{x-x_o}{w_1}\right)+1\right], \tag{9}$$

where $2A$ represents the total height difference across the jet, w_1 is a measure of the half-width of the jet, and $x_o(t)$ is the center latitude.

Although the jet location errors discussed in section 3 are non-Gaussian, in the mean for all satellite tracks, the jet location distribution is Gaussian and spatially symmetric. Therefore assume the probability density function for $x_o(t)$ is the distribution:

$$P(x_o) = \frac{1}{w_2\sqrt{\pi}}\exp\left[-\left(\frac{x_o-\overline{x_o}}{w_2}\right)^2\right]. \tag{10}$$

Thus a typical jet meanders about its mean position with a standard deviation w_2. Using the definition of the error function and combining (9) and (10), the mean SSH may be calculated as

$$\overline{h}(x) = A\left\{1+\frac{1}{w_2w_1\pi}\int_{-\infty}^{\infty}\int_0^x \exp\left[-\left(\frac{x'-x_o}{w_1}\right)^2\right]dx'\right\}$$
$$\left\{\exp\left[-\left(\frac{x_o-\overline{x_o}}{w_2}\right)^2\right]dx_o\right\}. \tag{11}$$

By switching the order of integration, (11) is reduced to the simple expression for $\overline{h}$:

$$\overline{h}(x) = A\left[\operatorname{erf}\left(\frac{x-\overline{x_o}}{\sqrt{w_1^2+w_2^2}}\right)+1\right]. \tag{12}$$

Correspondingly, the mean velocity is

$$\overline{v}(x) = -\frac{g}{f}\frac{2A}{\sqrt{\pi(w_1^2+w_2^2)}}\exp\left[-\left(\frac{x-\overline{x_o}}{\sqrt{w_1^2+w_2^2}}\right)^2\right]. \tag{13}$$

The mean squared height may be written

$$\overline{h^2} = \frac{A^2}{w_2\sqrt{\pi}}\int_{-\infty}^{\infty}\left[1+\operatorname{erf}\left(\frac{x-x_o}{w_1}\right)\right]^2$$
$$\exp\left[-\left(\frac{x_o-\overline{x_o}}{w_2}\right)^2\right]dx_o. \tag{14}$$

This expression is analytically difficult to work with because of the integrand containing erf^2, but it may be computed numerically using plausible values for w_1 and w_2 to produce an estimate of the variance of h, that is $\overline{h^2}-\overline{h}^2$, which is plotted as a solid line in Figure 15. A jet's height variance is spatially similar to its squared mean velocity, shown as the long-dashed line in Fig-

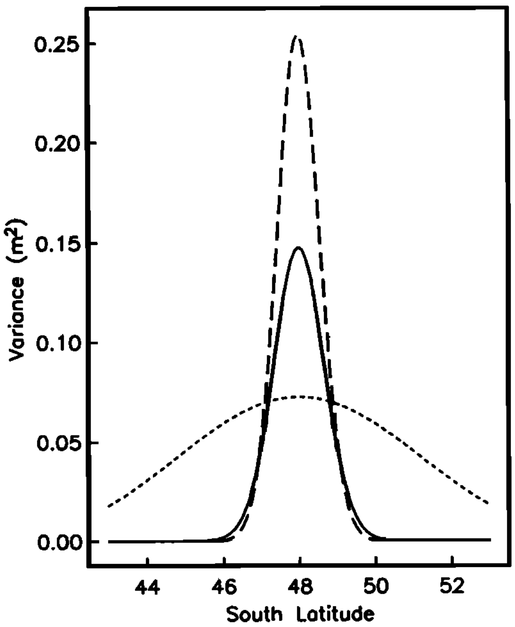

Figure 15. Predicted variance of altimeter height measurements. The solid line represents the SSH variance corresponding to a meandering Gaussian velocity jet, with parameters $w_1 = 0.5$ and $w_2 = 1.0$. The short-dashed line represents the variance of a ring modeled as a Gaussian height bump with parameters $w_1 = 0.5$ and $w_2 = 4.0$. For comparison, the long-dashed line shows the mean velocity squared ($\overline{v}^2$) for the meandering jet. By rescaling the measured height variance, we can obtain a plausible first approximation for $\overline{v}^2$.

ure 15. Both are basically Gaussian shapes centered at the mean axis of the current. Their widths differ by only a small margin. This suggests that by rescaling the amplitude of the height variance, we may obtain a reasonable proxy for the unknown mean velocity.

This result is a little clearer if we consider the limit where w_1 goes to zero, i.e., the jet becomes infinitesimally thin. In this case

$$\overline{v}(x) = -\frac{g}{f}\frac{2A}{\sqrt{\pi}w_2}\exp\left[-\left(\frac{x-\overline{x_o}}{w_2}\right)^2\right], \qquad (15)$$

and the variance is

$$\overline{h^2(x)} - \overline{h}(x)^2 = A^2\left[1 - \mathrm{erf}^2\left(\frac{x-\overline{x_o}}{w_2}\right)\right]. \qquad (16)$$

While the expression for the variance is not identical to the squared velocity, both attain a maximum value at $\overline{x_o}$ and their widths do not differ substantially.

Rings also have time-varying mesoscale features and may be mistaken for jets. However, if we assume that a typical ring moves substantially further than a jet, then its variance is likely to be smaller than the jet variance. To see this, parameterize the ring as the sum of an error function and a complimentary error function separated by the ring diameter $2d$,

$$h_{\mathrm{ring}}(x) = A\,\mathrm{erf}\left(\frac{x-x_o-d}{w_1}\right) - A\,\mathrm{erf}\left(\frac{x-x_o+d}{w_1}\right). \qquad (17)$$

Using the same probability distribution as above, the mean SSH is given by

$$\overline{h}(x) = A\,\mathrm{erf}\left(\frac{x-x_o-d}{\sqrt{w_1^2+w_2^2}}\right) - A\,\mathrm{erf}\left(\frac{x-x_o+d}{\sqrt{w_1^2+w_2^2}}\right). \qquad (18)$$

Again, the expression for the variance is best calculated numerically. The short dashed line in Figure 15 indicates that a typical widely meandering ring will have a broad flat variance with a smaller amplitude than the narrow jet variances. The shape and amplitude of bumps in the height variance provide a means to distinguish jet and eddy variance features. If the ring disappears some of the time, then its variance is correspondingly reduced.

The height variance is by no means a foolproof measure of the squared mean velocity. Local asymmetries in the jet distributions may alter the mean RMS height from the simple model description, so that the location of maximum variance does not coincide with the mean jet axis. Nonetheless, this approach provides a sensible way to use the available information as a first guess to feed into our error function model.

How well does this approximation work? Figure 16 shows an example of the height variance along one

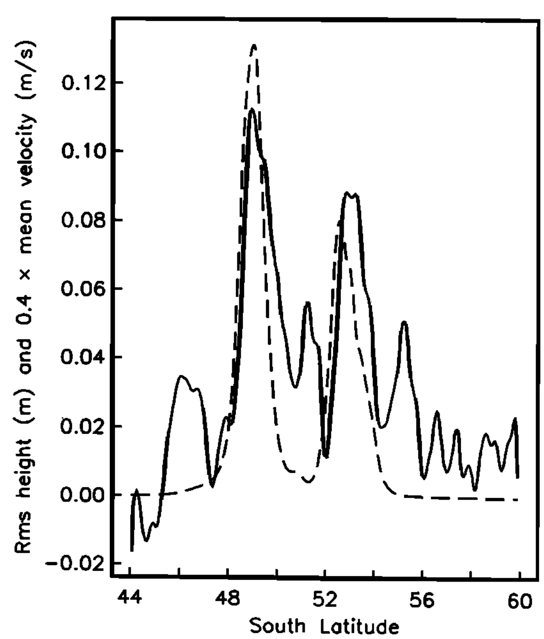

Figure 16. A comparison of the height standard deviation along track d001 (solid line) and estimated mean velocity from the Gaussian jet model (dashed line).

track compared to the mean velocity estimated using the Gaussian model. The synthetic velocity (dashed line) shows the SAF near 49.5°S and the PF near 53°S. The solid line represents the RMS SSH along the same ground track. With the selected scaling factor, the velocity of the SAF front is underestimated by about 25% and the velocity of the PF is overestimated by about 10%, which is sufficient for a first-order guess. The jet axes determined from the RMS height are located within 0.3° latitude of the jet maximum velocities.

Acknowledgments. This work has been completed with the guidance and encouragement of my advisor, K. Kelly. T. Joyce, S. Lentz, and M. McCartney provided valuable comments on earlier drafts of this paper. In addition this work benefitted from discussions with B. Qiu and C. Wunsch and from the computer assistance of M. Caruso. Geosat data were provided by the National Oceanographic Data Center. D. Olbers made his gridded data set publicly available, and B. Huber provided the gridded atlas data of *Gordon et al.* [1982]. Some of the objective mapping was performed using supercomputer facilities at the National Center for Atmospheric Research, which is operated by the University Corporation for Atmospheric Research and is sponsored by the National Science Foundation. Funding for this research was provided by an Office of Naval Research graduate student fellowship and National Aeronautics and Space Administration contract NAGW-1666. This is WHOI contribution 8524.

References

Bretherton, F.P., R.E. Davis, and C.B. Fandry, A technique for objective analysis and design of oceanographic experiments applied to MODE-73, *Deep-Sea Res., 23*, 559-582, 1976.

Callahan, J.E., Velocity structure and flux of the Antarctic Circumpolar Current south of Australia, *J. Geophys. Res., 76*, 5859–5864, 1971.

Campbell, J.W., Evaluation of Geosat data and application to variability of the northeast Pacific Ocean, *Tech. Rep. WHOI-88-40*, Woods Hole Oceanogr. Inst., Woods Hole, Mass., 1988.

Caruso, M.J., Z. Sirkes, P.J. Flament, and M.K. Baker, Altimeter processing tools for analyzing mesoscale ocean features, *Tech. Rep. WHOI-90-45*, Woods Hole Oceanogr. Inst., Woods Hole, Mass., 1990.

Chelton, D.B., WOCE/NASA Altimeter Algorithm Workshop, U.S. WOCE Tech. Rep. *No. 2*, 70 pp., U.S. Plann. Off. for World Ocean Circ. Exp., College Station, Tex, 1988.

Chelton, D.B., M.G. Schlax, D.L. Witter, and J.G. Richman, Geosat altimeter observations of the surface circulation of the Southern Ocean, *J. Geophys. Res., 95*, 17,877–17,903, 1990.

Cheney, R.E., N.S. Doyle, B.C. Douglas, R.W. Agreen, L. Miller, E.L. Timmerman, and D.C. McAdoo, The complete Geosat altimeter GDR handbook, *NOAA Manual NOS-NGS-7*, 79 pp., U.S. Govt. Print. Office, Washington, D.C., 1991.

Gordon, A.L., Structure of Antarctic waters between 20°W and 170°W, *Antarctic Map Folio Ser.*, folio 6, edited by V. Bushnell, Am. Geogr. Soc., New York, 1967.

Gordon, A.L., On the interaction of the Antarctic Circumpolar Current and the Macquarie Ridge, in *Antarctic Oceanology II: The Australian–New Zealand Sector, Antarctic Res. Ser.*, vol. 19, edited by D.E. Hayes, pp. 71–78, AGU, Washington, D.C., 1972.

Gordon, A.L., E. Molinelli, and T. Baker, Large-scale relative dynamic topography of the Southern Ocean, *J. Geophys. Res., 83*, 3023–3032, 1978.

Gordon, A.L., E.J. Molinelli, and T.N. Baker, *Southern Ocean Atlas*, Columbia University Press, New York, 1982.

Jacobs, S.S., and D.T. Georgi, Observations on the southwest Indian/Antarctic Ocean, in *A Voyage of Discovery*, ed. by M. Angell, pp. 43–84, Pergamon, New York, 1977.

Johnson, T.J., R.H. Stewart, C.K. Shum, and B.D. Tapley, Distribution of Reynolds stress carried by mesoscale variability in the Antarctic Circumpolar Current, *Geophys. Res. Lett., 19*, 1201–1204, 1992.

Joyce, T.M., and S.L. Patterson, Cyclonic ring formation at the Polar Front in the Drake Passage, *Nature, 265*, 131–133, 1977.

Kelly, K.A., The meandering Gulf Stream as seen by the Geosat altimeter: Surface transport, position, and velocity variance from 73° to 46°W, *J. Geophys. Res., 96*, 16,721–16,738, 1991.

Kelly, K.A., and S.T. Gille, Gulf Stream surface transport and statistics at 69°W from the Geosat altimeter, *J. Geophys. Res., 95*, 3149–3161, 1990.

Kelly, K.A. and D.R. Watts, Monitoring Gulf Stream transport by radar altimeter and inverted echo sounders, *J. Phys. Oceangr., 24*, 1080–1084, 1994.

Kelly, K.A., T.M. Joyce, D.M. Schubert, and M.J. Caruso, The mean sea surface height and geoid along the Geosat subtrack from Bermuda to Cape Cod, *J. Geophys. Res., 96*, 12,699–12,709, 1991.

Morrow, R., J. Church, R. Coleman, D. Chelton, and N. White, Eddy momentum flux and its contribution to the Southern Ocean momentum balance, *Nature, 357*, 482–484, 1992.

Nowlin, W.D., Jr., and M. Clifford, The kinematic and thermohaline zonation of the Antarctic Circumpolar Current at Drake Passage, *J. Mar. Res., 40S*, 481–507, 1982.

Nowlin, W.D., Jr., and J.M. Klinck, The physics of the Antarctic Circumpolar Current, *Rev. Geophys., 24*, 469–491, 1986.

Olbers, D., V. Gouretski, G. Seiss, and J. Schröter, *Hydrographic Atlas of the Southern Ocean*, Alfred Wegener Institute, Bremerhaven, Germany, 1992.

Orsi, A. H., On the extent and frontal structure of the Antarctic Circumpolar Current, Ph.D. thesis, Texas A&M University, College Station, Tex., 1993.

Park, Y.-H., L. Gambéroni, and E. Charriaud, Frontal structure and transport of the Antarctic Circumpolar Current in the south Indian Ocean sector, 40°–80°E, *Mar. Chem., 35*, 45–62, 1991.

Park, Y.-H., L. Gambéroni, and E. Charriaud, Frontal structure, water masses, and circulation in the Crozet Basin, *J. Geophys. Res., 98*, 12,361–12,385, 1993.

Peterson, R.G., and T. Whitworth, The subantarctic and polar fronts in relation to deep water masses through the southwestern Atlantic, *J. Geophys. Res., 94*, 10,817–10,838, 1989.

Peterson, R.G., W.D. Nowlin, and T. Whitworth, Generation and evolution of a cyclonic ring at Drake Passage in early 1979, *J. Phys. Oceanogr., 12,* 712–719, 1982.

Press, W.H., B.P. Flannery, S.A. Teukolsky, and W.T. Vetterling, *Numerical Recipes,* 818 pp., Cambridge University Press, New York, 1986.

Qiu, B., Recirculation and seasonal change of the Kuroshio from altimetry observations, *J. Geophys. Res., 97,* 17,801–17,811, 1992.

Qiu, B., Kelly, K.A., and T.M. Joyce, Mean flow and variability of the Kuroshio Extension from Geosat altimetry data, *J. Geophys. Res., 96,* 18,491–18,507, 1991.

Read, J.F., and R.T. Pollard, Structure and transport of the Antarctic Circumpolar Current and Agulhas Return Current at 40°E, *J. Geophys. Res., 98,* 12,281–12,295, 1993.

Reid, J.L., Jr. On the temperature, salinity, and density differences between the Atlantic and Pacific oceans in the upper kilometer, *Deep-Sea Res., 7,* 265–275, 1961.

Reid, J.L., On the total geostrophic circulation of the South Pacific Ocean: Flow patterns, tracers and transports, *Prog. Oceanogr., 16,* 1–61, 1986.

Reid, J.L., On the total geostrophic circulation of the South Atlantic Ocean: Flow patterns, tracers and transports, *Prog. Oceanogr., 23,* 149–244, 1989.

Savchenko, V.G., W.J. Emery, and O.A. Vladimirov A cyclonic eddy in the Antarctic Circumpolar Current south of Australia: Results of Soviet-American observations aboard the R/V *Professor Zubov, J. Phys. Oceanogr., 8,* 825–837, 1978.

Stammer, D., and C.W. Böning, Mesoscale variability in the Atlantic Ocean from Geosat altimetry and WOCE high-resolution numerical modeling, *J. Phys. Oceanogr., 22,* 732–752, 1992.

Wearn, R.B., Jr., and D. J. Baker Jr., Bottom pressure measurements across the Antarctic Circumpolar Current and their relation to the wind, *Deep-Sea Res., 27A,* 875–888, 1980.

Whitworth, T., III, Monitoring the transport of the Antarctic Circumpolar Current at Drake Passage, *J. Phys. Oceanogr., 13,* 2045–2057, 1983.

Whitworth, T., III, and R.G. Peterson, Volume transport of the Antarctic Circumpolar Current from bottom pressure measurements, *J. Phys. Oceanogr., 15,* 810–816, 1985.

Whitworth, T., III, W.D. Nowlin Jr., and S.J. Worley, The net transport of the Antarctic Circumpolar Current through Drake Passage, *J. Phys. Oceanogr., 12,* 960–971, 1982.

S. T. Gille, Department of Physical Oceanography, Woods Hole Oceanographic Institution, Woods Hole, MA 02543. (e-mail: Internet: gille@solarmax.whoi.edu)

(Received February 22, 1994; revised May 3, 1994; accepted May 3, 1994.)